CMS PAS FSQ-13-006

CMS Physics Analysis Summary

Contact: cms-pag-conveners-fsq@cern.ch

2013/12/19

Measurement of the inelastic proton-lead cross section at $\sqrt{s_{\mathrm{NN}}} = 5.02\,\mathrm{TeV}$

The CMS Collaboration

Abstract

A measurement of the inelastic proton-lead (pPb) cross section at a nucleon-nucleon centre-of-mass energy of 5.02 TeV is presented using the CMS detector at the LHC. Inelastic collisions are tagged using the forward calorimeters at pseudorapidities $3 < |\eta| < 5$. Two different event selections are used: (i) a coincidence of both sides of the detector, and (ii) a single-sided event selection. These two selections have different sensitivity to contributions from photon induced (γp) collisions and hadronic diffractive interactions. The value of the hadronic inelastic cross section is measured within the CMS acceptance and extrapolated to its total value. The photon-induced contribution is subtracted. The final result is $\sigma_{\mathrm{inel}} = 2.06 \pm 0.08\,\mathrm{b}$. The uncertainty is dominated by the luminosity determination. This measurement of the inelastic cross section is consistent with the expectation from the Glauber approach.

1 Introduction

The total inelastic cross section for particle production in hadronic collisions is arguably the most inclusive observable open to measurement, yet one of the least theoretically clear-cut quantities as it cannot be determined from first-principles calculations of the theory of the strong interaction, quantum chromodynamics (QCD). At LHC energies, the largest fraction of the particles produced in hadronic interactions comes from the hadronisation of quarks and gluons ("minijets") produced in semi-hard scatterings with exchanged momenta of 1–3 GeV/c [1]. Yet, a non-negligible fraction of the inelastic cross section arises from soft diffractive interactions. Furthermore, in the case of interactions involving nuclear beams one has to consider other non-perturbative aspects such as the transverse overlap of the colliding objects and possible coherent effects in multiple-scattering processes. Such dynamics are phenomenologically described, for example, in Glauber [2, 3] or Gribov-Regge [4] approaches. Those models are based on the optical theorem and the underlying conservation of probability. An additional issue in nuclear collisions is the large inelastic cross sections from photo-hadronic interactions, that scale with the square of the charge of the ion (Z^2). In the present analysis photo-nuclear collisions are explicitly subtracted.

Parametrisation of cross section data is an essential input to Monte Carlo event generators that are designed for modelling high-energy hadronic and nuclear collisions using the perturbative minijet formalism (such as PYTHIA [5] for proton-proton and HIJING [6] for heavy-ion collisions). Alternative event generators that are commonly used in the study of high-energy interactions of cosmic rays with the atmosphere, such as EPOS [7] and QGSJetII [8], use the Gribov-Regge framework to combine the prediction of hadronic and nuclear cross sections with the construction of scattering amplitudes [9, 10].

For any model that calculates nuclear interactions, the Glauber approach is crucial to compute many quantities related to the geometrical overlap of the colliding ions (nuclear overlap function, number of nucleon-nucleon collisions and participant nucleons...) [11, 12]. Most of the Glauber-based models, however, neglect the effect of possible nucleon-nucleon correlations in the nucleus: this leads to fewer collisions at very small impact parameters (central collisions) and more collisions at larger impact parameters (peripheral collisions). This effect, called *anti-screening*, increases the nuclear cross section. The other most relevant effect neglected by the standard Glauber model is the impact of diffraction in the context of multiple scatterings [13]. It is possible that a nucleon is excited during the multiple scattering process but falls back to the ground state before the scattering process is terminated. In such cases the final state is not distinguishable from a pure elastic final state. Such an *inelastic screening* has the effect of reducing the final cross section. The screening and anti-screening effects result in opposite-sign modifications on the order of 10 % on the inelastic cross section. These corrections are verified with measurements at lower energies [14, 15]. Precise experimental measurements of the proton-nucleus cross section at the LHC can shed light on the relative importance and the magnitude of these effects and whether their coincidental cancellation applies to all colliding systems and/or at all energies.

In this analysis the inelastic proton-lead cross section at $\sqrt{s_{\mathrm{NN}}}$ = 5.02 TeV is measured with the CMS experiment and is compared to model predictions and experimental data at lower energies. This result provides another controlled test of the Glauber model at TeV-energies, and complements for example the comparison of W boson production in lead-lead and proton-proton (pp) data at $\sqrt{s_{\mathrm{NN}}}$ = 2.76 TeV [16]. The measurement of the inelastic proton-lead cross section is also important in the context of the measuring the proton-air cross section with cosmic-ray experiments. The Pierre Auger Collaboration recently published the measurement of the proton-air cross section [17] at $\sqrt{s_{\text{NN}}} = 57\,\text{TeV}$ and used an extended Glauber model with inelastic screening [13, 18] in order to relate this measurement to pp cross sections.

2 Experimental Setup

The central part of the CMS experiment is the 3.8 T solenoid magnet, which comprises the silicon tracker, electromagnetic calorimeter and also most parts of the hadronic calorimeter. A general description of the CMS detector can be found elsewhere [19]. Here, only the subdetectors relevant in the context of this analysis are highlighted.

Inelastic collisions are tagged using the hadronic forward (HF) detector [20] that covers the pseudorapidity interval $3 < |\eta| < 5$ with one calorimeter on either side of the interaction region. The calorimeter is composed of quartz fibres in a steel matrix with a 0.175×0.175 segmentation in the azimuthal angle ϕ and pseudorapidity η. The quartz fibres pick up the Cherenkov light produced by the charged component of the showers. This light is then measured by photodetector tubes. The hadronic and electromagnetic signal of each segment is combined to form a *tower* signal. In the following, the single highest signal for a tower in the HF calorimeters is used for the analysis.

Beam-gas collisions and electronic noise backgrounds are studied with events triggered by dedicated capacitive beam pickup detectors (BPTX). These detectors are installed ± 175 m away from the interaction point and detect the presence of particle bunches from the beam. The so called "zero bias data" is obtained by triggering on the coincidence of BPTX signals from both beams while, in order to study the effect of the electronic noise and beam background, a fraction of events is recorded by triggering on the absence of either one or both BPTX signals.

3 Luminosity

This analysis uses proton-lead collision data collected in the first weeks of 2013. The data were collected with the proton beam injected both clockwise and counter-clockwise. These two configurations are called lead-proton and proton-lead collisions.

Because of the different energies of the two beams the nucleon-nucleon centre-of-mass in proton-lead collisions is not at rest. The results are presented in the laboratory frame, where the proton beam travels in the positive η direction.

The data was recorded during LHC fills with 296 colliding bunch pairs, each lead bunch contains on average 7.2×10^9 and each proton bunch 15.4×10^9 particles. The bunch spacing is 200 ns.

Two short data taking periods during the proton-lead and lead-proton runs were dedicated to determining the absolute luminosity scale for the complete data taking period, using van-der-Meer scans [21].

The value of luminosity can be expressed using any visible cross section σ_{vis} via the following relationship:

$$L(t) = R(t)/\sigma_{\text{vis}}\,, \tag{1}$$

where $R(t)$ is the observed interaction rate at the time t.

For the van-der-Meer method the instantaneous luminosity $L(t)$ is expressed as a function of the interaction rate as

$$L(t) = \nu N_1 N_2 \, R(t) \, A_{\mathrm{eff}}^{-1} \, , \tag{2}$$

where $\nu = 11246$ Hz is the LHC orbit frequency, N_i is the beam intensity of beam i, and the quantity

$$A_{\mathrm{eff}} = \int R(\Delta_x, \Delta_y) \, d\Delta_x \, d\Delta_y = \frac{\left[\int R(\Delta_x, 0) \, d\Delta_x\right] \times \left[\int R(0, \Delta_y) \, d\Delta_y\right]}{R(0,0)} \tag{3}$$

can be interpreted as an effective overlapping area of the two beams. The rate R is expressed as a function of the beam separation Δ for each x and y-direction.

The rate was obtained using HF as a luminometer and exploits the fact that

$$R(\Delta_x, \Delta_y) = \mathrm{const} \times (-\log p_0) \, , \tag{4}$$

where p_0 is the average fraction of empty cells in the calorimeter. To increase linearity of the rate, the coverage is limited to four azimuthal (2π) rings in the range $3.5 < |\eta| < 4.2$. The rate was measured at 25 values of each Δ_x and Δ_y. The integral in Eq. (3) is obtained by fitting the values as a function of separation Δ. Empirical functions are used for fitting and describing the beam shape. Here, a *supergaussian* function is employed, that can describe the observed rectangular beam shapes of the proton-lead beams better than a Gaussian function. The function is motivated in [22] where possible reasons for a rectangular beam shape are given. However, since the reasons have not yet been investigated for the current data, the fit model introduces the largest systematic uncertainty.

The luminosity has been determined by van-der-Meer scans with a systematic uncertainty of ±3.5% for the proton-lead (pPb) as well as the lead-proton (Pbp) beam direction. A similar study of the uncertainties was performed for the method of pixel cluster counting in [23], for which the uncertainties are determined in the same way. Only the determination of luminometer-specific uncertainties differ in the reference.

With the CMS experiment an integrated luminosity of about $(20.7 \pm 0.7)\ \mathrm{nb}^{-1}$ $\left[(14.0 \pm 0.5)\ \mathrm{nb}^{-1}\right]$ for proton-lead [lead-proton] collisions was recorded .

4 Analysis

The inelastic cross section is determined by counting the number of inelastic events and relating it to the integrated luminosity $\mathcal{L}$:

$$\sigma_{\mathrm{inel}} = \frac{N_{\mathrm{inel}}}{\mathcal{L}} \, . \tag{5}$$

Using MC simulations, N_{vis}, the number of visible events that pass a selection for inelastic events, is corrected to account for detector acceptance limitations and inefficiencies to obtain the true number of inelastic events N_{inel}.

4.1 Simulation

Three event generators, based on Regge-Gribov (EPOS-LHC, QGSJETII-04) or Glauber (HIJING) theory combined with perturbative QCD are employed to generate proton-nucleus collisions. A GEANT4 simulation is used to model the experimental response of the detector.

During high luminosity data taking in 2012 the detector suffered from radiation damage in particular at high pseudorapidities. To take this into account, the simulated response is rescaled to match the data. The rescaling factors range from 1 to about 1.5 depending on the pseudorapidity. With this procedure, a good and accurate simulation of the event selection procedure is reached. The influence of rescaling on the uncertainty of the final result is discussed in Section 5.

Electromagnetic interactions of lead ions with the incoming protons are simulated with the STARLIGHT generator [24]. The photon-hadron interaction ($\gamma^* + \text{parton} \rightarrow \text{X}$) is calculated using a combination of the STARLIGHT photon fluxes with the DPMJET 3 [25] as well as PYTHIA frameworks.

4.2 Event Selection

At inelastic collisions most of the released energy is carried by particles that are boosted towards high pseudorapidities. Thus, the CMS forward calorimeters are well suited to tag these events.

The analysis is performed for two different event selections, both relying on the HF tower with the largest measured energy deposit:

- The **single-arm event selection** relies on a single sided HF event selection. This has the largest possible acceptance for inelastic events. In particular it has a high acceptance of single-diffractive events. At the same time, it also has an increased acceptance for photo-nuclear events. Furthermore, the absence of a coincidence requirement leads to an increased noise level, which requires larger values for the event selection energy threshold.
- The **double-arm event selection** is based on the coincidence requirement of both HF detectors. This reduces the noise rate and allows for smaller values of energy thresholds for the event selection. The coincidence requirement also removes efficiently photo-nuclear events. However, also a fraction of the single-diffractive events is removed. Hence, the acceptance towards inelastic collisions is reduced in the double-arm case.

Defining the highest energy in a tower of the HF calorimeter positioned at positive (negative) rapidity, $E_{\text{HF+}}$ ($E_{\text{HF-}}$), one can define the following variable:

$$E_{\text{HF}} = \begin{cases} \max(E_{\text{HF+}}, E_{\text{HF-}}) & \text{(single-arm selection)} \\ \min(E_{\text{HF+}}, E_{\text{HF-}}) & \text{(double-arm selection)}\,. \end{cases} \tag{6}$$

Figure 1 shows the distribution of E_{HF} for data collected with the zero bias and noise triggers. The number of separately recorded noise events is scaled to compensate trigger pre-scales. With this definition of E_{HF}, the selection criteria for single and double arm can be defined by requiring E_{HF} larger than a threshold energy. Studying both selections has the advantage of exploiting different sensitivities to the various necessary corrections to N_{vis}. For this analysis the single-arm selection has a smaller acceptance correction ($\approx 6\%$) than the double-arm selection

(≈ 9%), but it requires a larger correction owing to photo-nuclear events. The noise as well as the contribution from photon-proton collisions can be reduced by increasing the threshold energy. Both are considered background to measuring N_{inel}. To apply an optimal threshold energy for the event selection, in the following the efficiency and the amount of background events are studied in detail.

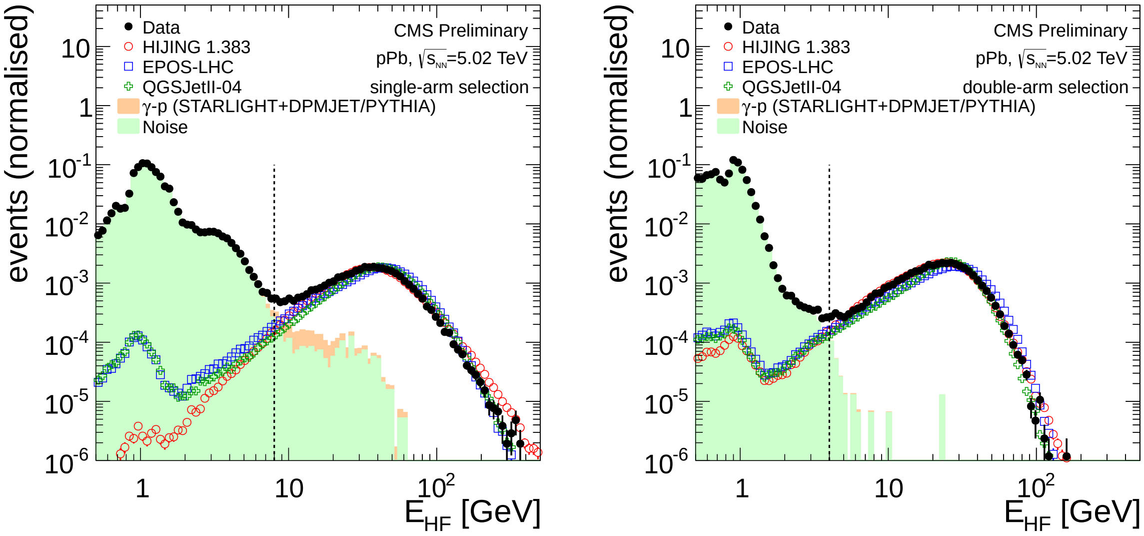

Figure 1: Distribution of E_{HF}. The noise rate (random trigger with empty bunch crossings) is matched to the zero bias trigger rate. The average of γp simulated with STARLIGHT +DPMJET and STARLIGHT +PYTHIA is added to the background as well. Three hadronic interaction models (EPOS-LHC, HIJING, and QGSJETII-04) are also shown. These models are normalised to the number of zero bias events above 10 GeV, where the contribution from the background is low. The vertical lines represent the threshold energies used in this analysis.

In Fig. 2 the fraction of events passing the two selection criteria according to Eq. (6) is shown as a function of a threshold energy E_{HF} for hadronic interactions (top) and photo-nuclear interactions and noise (bottom). For both selection criteria the noise fraction drops rapidly compared to the fraction of selected inelastic events. This information is obtained from studying randomly triggered, non-colliding-beam events. Photo-nuclear processes have only a small dependence on the energy threshold for the single-arm selection but the contribution can be greatly reduced with the double-arm selection even at a small energy threshold.

In Section 4.3 it is shown that one can correct for the background contribution, hence, a large fraction of hadronic inelastic events passing the selection is preferred. The selected thresholds on E_{HF} for the single-arm and double-arm event selection are 8 GeV and 4 GeV, respectively. At this threshold energy the background and the hadronic inelastic contribution are approximately equal.

4.3 Corrections

Four corrections need to be taken into account when counting the number of events: misidentified noise events, contribution from photo-nuclear γp interactions, contribution from pileup (multiple collisions in one event), and the extrapolation to full phase space.

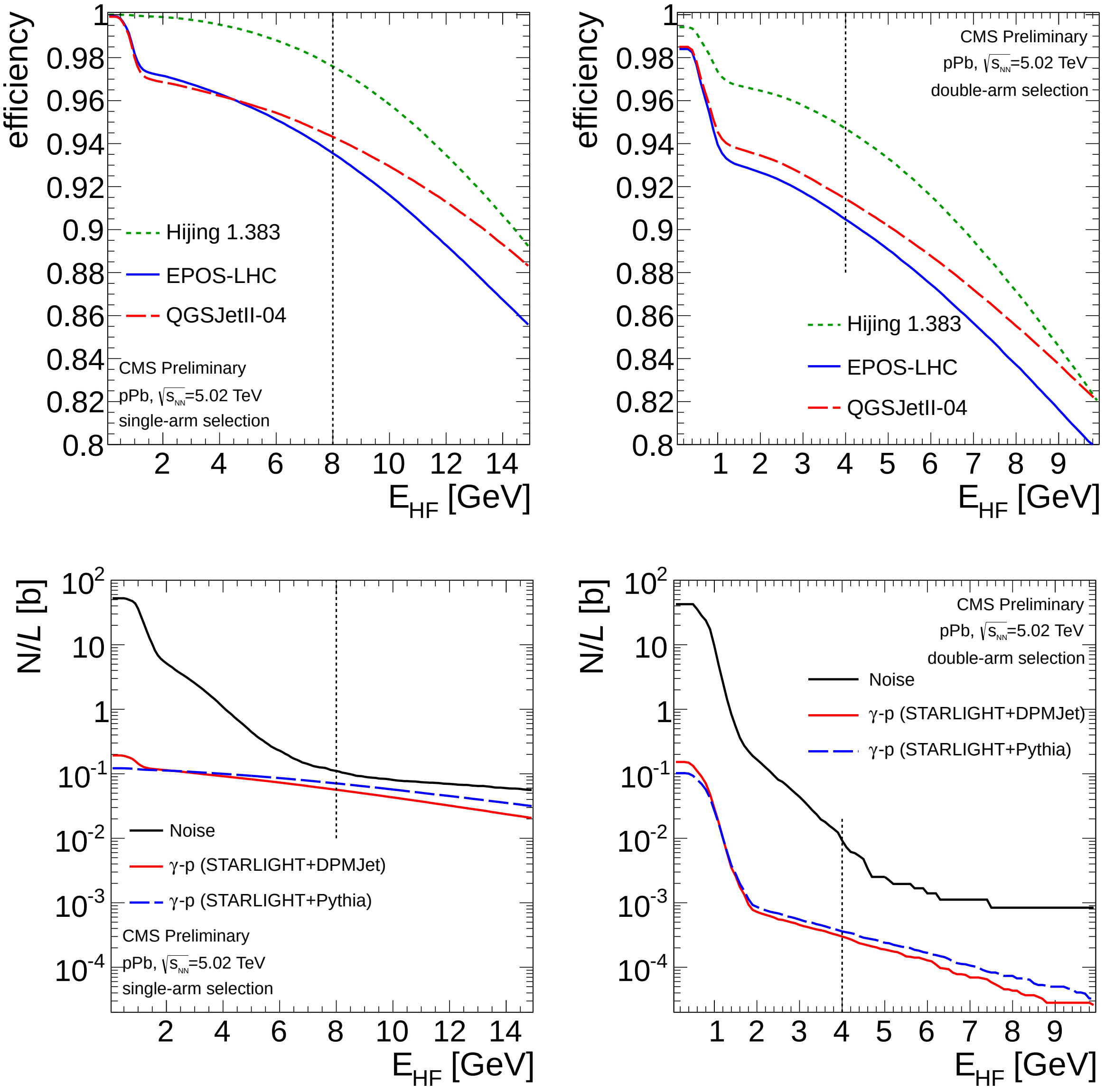

(a) single-arm selection

(b) double-arm selection

Figure 2: Top panel: Efficiency for different selection thresholds for E_{HF} for three hadronic interaction models are shown. Bottom panel: Visible cross section for noise (randomly triggered, empty bunch crossings) events and photo-nuclear events passing the selection. The vertical lines represent the threshold energies used in this analysis.

Acceptance and Diffractive Dissociation Contributions

For small transverse momentum transfers to diffractive systems, the produced particles are boosted to high $|\eta|$. The maximum value of pseudorapidity covered by HF is at $|\eta| = 5$. Thus, a fraction of the particles created diffractively will not hit HF and leave the experiment undetected. Besides these single-diffractive (SD) reactions, in which just one of the participating nucleons (the proton or a nucleon from the lead) disintegrates, there is also the possibility that both nucleons produce a diffractive system, which is called double-diffraction (DD). Furthermore, double pomeron exchange can lead to isolated exclusive central particle production, which is called central-diffraction (CD).

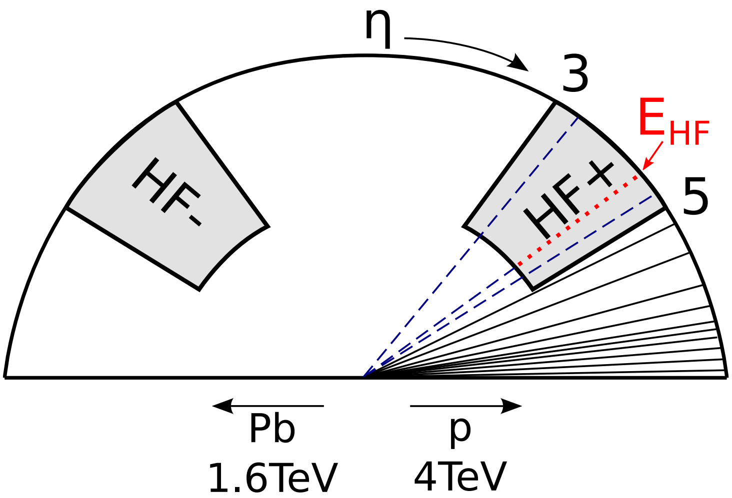

Figure 3: Illustration of a single-diffractive event where the proton disintegrates and three particles (dashed lines) are within the acceptance of the HF calorimeter. The particle with the highest energy (dotted line) determines E_{HF}.

In Fig. 3 one can see a cartoon where a single-diffractive event is registered in only one of the HF detectors. This type of event can only be selected by the single-arm event selection. For all types of diffractive collisions a fraction of events cannot be registered. The same applies to a smaller extent to non-diffractive (ND) collisions. To quantify this, the energy in the acceptance of HF is studied at generator level and compared to detector simulation. The study explains how the diffractive and non-diffractive event types contribute to the value of efficiency smaller than unity seen in Fig. 2.

For the three Monte Carlo generators used to simulate pPb events, Fig. 4 shows the energy distribution E_{HF} for diffractive and non-diffractive event classes. At low energies there is a higher fraction of diffractive events. The diffractive events have almost no contribution to the distribution for $E_{\mathrm{HF}} > 100\,\mathrm{GeV}$ for the single-arm and $E_{\mathrm{HF}} > 40\,\mathrm{GeV}$ for double-arm selection. At low energies (< 1 GeV) these events dominate. Table 1 shows the remaining fraction of events after the event selection for different MC generators. EPOS-LHC predicts more than twice as many DD collisions than QGSJETII-04, which instead has a higher SD contribution. The requirement on the single-arm energy roughly halves the single diffractive contribution but the double-arm requirement reduces it by more than a factor of four. The influence of the event selection on non-diffractive events is smaller ($< 3\%$). The total loss is therefore similar to the loss due to diffractive events. For HIJING this information is not available.

The fraction of events passing the selection criteria for all event types (column "$\sum$") corresponds to the efficiency to select hadronic inelastic events within the finite acceptance of CMS.

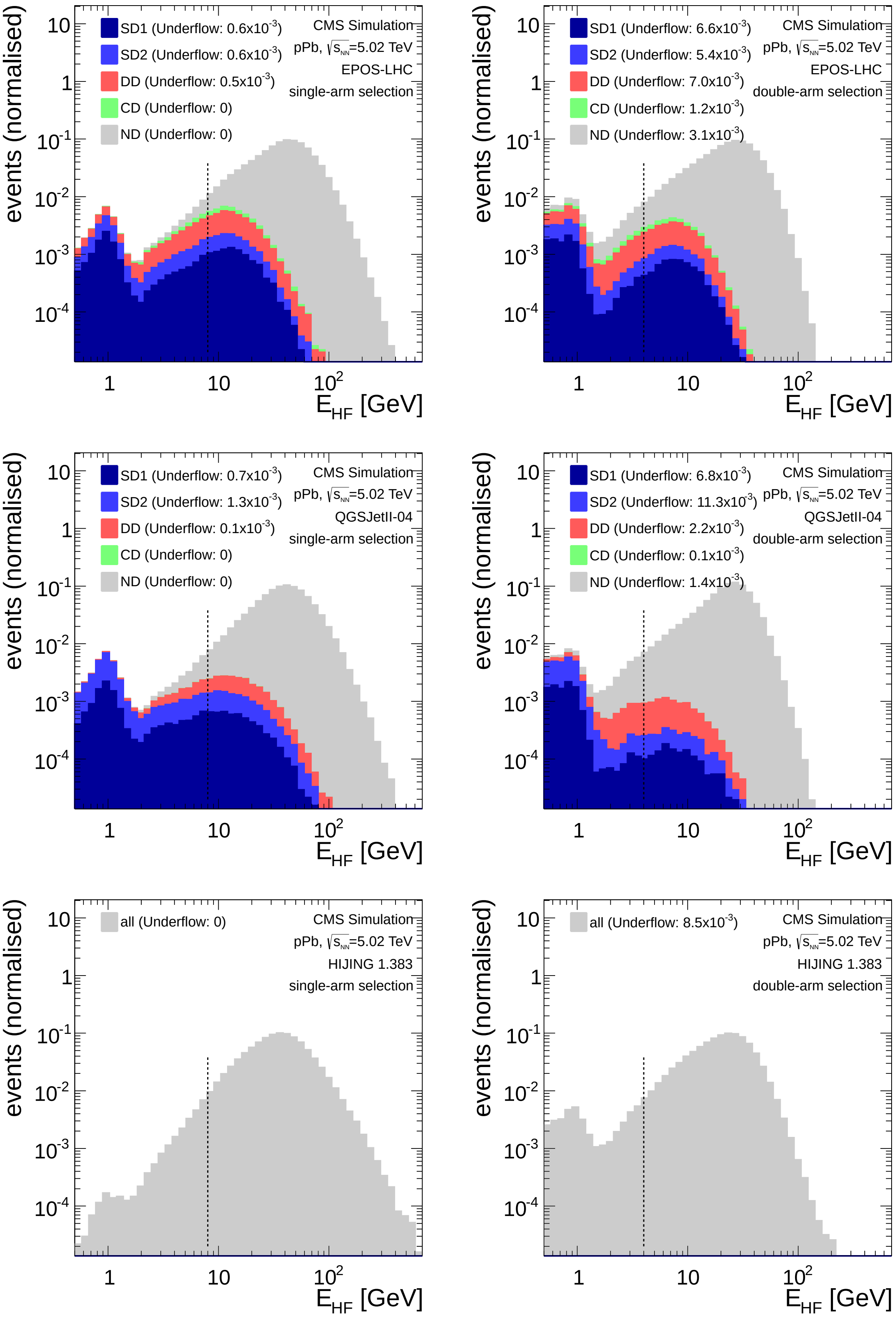

Figure 4: Distribution of $E_{\rm HF}$ for three MC generators: EPOS-LHC (top), QGSJETII-04 (middle) and HIJING (bottom). The single-arm selection is on the left side and the double-arm selection on the right side. Five stacked categories of inelastic collisions are shown: single-diffractive where the lead ion (SD1) or the proton (SD2) dissociates, double-diffractive (DD), central-diffractive (CD), and non-diffractive (ND) events are shown for each.

Table 1: Fractions of events in each type of collision before and after the two triggers $E_{\mathrm{HF}} > 8$ GeV (single-arm) and $E_{\mathrm{HF}} > 4$ GeV (double-arm). Four types of events are considered: single-diffraction (SD), double-diffraction (DD), central-diffraction (CD), and non-diffractive (ND) events. The last two columns show the ratios double-arm/single-arm selection for the MC and data. The latter corresponds to $\sigma_{\mathrm{vis,had}}$ (double-arm)/$\sigma_{\mathrm{vis,had}}$ (single-arm) defined in Section 4.4.

Model	Selection	SD [%]	DD [%]	CD [%]	ND [%]	$\sum$ [%]	Ratio (MC)	Ratio (Data)
EPOS-LHC	No selection	4.5	4.5	1.1	90.0	100	-	0.966
	Single-arm	1.7	2.4	0.7	88.9	93.7	0.969	
	Double-arm	1.1	1.8	0.5	87.3	90.8		
HIJING	No selection	-	-	-	100	100	-	
	Single-arm	-	-	-	97.7	97.7	0.972	
	Double-arm	-	-	-	94.9	94.9		
QGSJETII-04	No selection	5.1	1.8	0.0	93.1	100	-	
	Single-arm	1.2	1.2	0.0	92.0	94.4	0.971	
	Double-arm	0.3	0.7	0.0	90.7	91.7		

Figure 2 shows ϵ_{acc} for different threshold energies. For the values of thresholds used in this analysis, the efficiency is determined as the average of EPOS-LHC and QGSJETII-04:

$$\epsilon_{\mathrm{acc}} = \begin{cases} 0.939 \pm 0.005 & (\text{single-arm } E_{\mathrm{HF}} > 8\,\mathrm{GeV}) \\ 0.910 \pm 0.014 & (\text{double-arm } E_{\mathrm{HF}} > 4\,\mathrm{GeV})\,. \end{cases} \tag{7}$$

HIJING, which lacks double-diffraction and mass dependence of the diffractive cross section, is not used for the efficiency correction. The correction factor $1/\epsilon_{\mathrm{acc}}$ is used to extrapolate the value of the cross section to the full phase space. The uncertainty on ϵ_{acc} is obtained from the difference $\Delta\epsilon_{\mathrm{acc}}$ of the models EPOS-LHC and QGSJETII-04. The uncertainty is taken as the average of $|\Delta\epsilon_{\mathrm{acc}}|$ obtained by changing the cut on E_{HF} in steps of 0.1 GeV between 2 and 10 GeV.

The last two columns of Table 1 show the the ratios of $\sigma_{\mathrm{vis,had}}$ (double-arm)/$\sigma_{\mathrm{vis,had}}$ (single-arm) for data and MC. Because of the different sensitivities of the selections to diffractive events, the ratio will decrease with a rising number of diffractive events. To match the ratio of the MC programs to data, one would have to artificially increase the diffractive cross section by 1.12 and 1.50 for EPOS-LHC and QGSJETII-04, respectively. This would increase σ_{inel} by 1.5% (2.0%) for single-arm (double-arm) selection. This effect enters as one of the systematic uncertainties listed in Section 5 but is not applied in Eq. 7.

The extreme case of enhancing the diffractive cross section by a factor of two would result in an increase of σ_{inel} of 5.1% (6.7%) for single-arm (double-arm) selection. However, since the ratio $\sigma_{\mathrm{vis,had}}$ (double-arm)/$\sigma_{\mathrm{vis,had}}$ (single-arm) decreases to a value (95.4% for EPOS-LHC and 96.0% for QGSJETII-04) below the ratio seen in data, the extreme case is not taken into account in the uncertainties of this analysis.

Detector Noise

Electronic noise and beam gas collisions generate energy depositions in the HF detector that are not related to inelastic collisions. This contributes mostly to the low-energy part of the energy distribution but, depending on the selection threshold value, can be misidentified as signal. With, the fraction f_{noise} of randomly read out no-beam events that survive the selection requirement, the number of noise events is $N_{\text{noise}} = N_{\text{ZeroBias}} f_{\text{noise}}$, where N_{ZeroBias} is the number of events recorded by the zero bias trigger. Furthermore, if N_{inel} is the number of inelastic collisions, there will also be $N_{\text{inel+noise}} = N_{\text{inel}} f_{\text{noise}}$ events that contain both, an inelastic collision and significant contribution from noise. In Fig. 2 (bottom) $N_{\text{noise}}/\mathcal{L}$ is shown for different selection thresholds. Applying the event selection one obtains:

$$f_{\text{noise}} = \begin{cases} (2.0 \pm 0.5) \times 10^{-3} & (\text{single-arm } E_{\text{HF}} > 8\,\text{GeV}) \\ (1.8 \pm 0.8) \times 10^{-4} & (\text{double-arm } E_{\text{HF}} > 4\,\text{GeV})\,. \end{cases} \tag{8}$$

and

$$\frac{N_{\text{noise}}}{\mathcal{L}} = \begin{cases} (102 \pm 25)\ \text{mb} & (\text{single-arm } E_{\text{HF}} > 8\,\text{GeV}) \\ (9 \pm 3)\ \text{mb} & (\text{double-arm } E_{\text{HF}} > 4\,\text{GeV})\,. \end{cases} \tag{9}$$

The uncertainties are derived from run-by-run variations. Subtracting the photo-nuclear contribution introduces a correction of about 5.4% and 0.5% for N_{vis} for single-arm and double-arm selection, respectively.

Pileup

Bunches of the two beams contain more than one proton or nucleus and it is therefore possible for multiple interactions to occur in a single bunch crossing. This effect depends on the cross section. The discrete distribution of the number, i, of collisions per bunch crossing follows the Poisson law

$$\text{Pois}(i;\lambda) = \frac{\lambda^i}{i!} e^{-\lambda}\,, \tag{10}$$

where λ is the interaction probability. A bunch crossing with i interactions can be detected with the probability

$$P_i = 1 - (1 - \epsilon_{\text{acc}})^i\,. \tag{11}$$

This equation neglects possible correlations between simultaneous events. Namely in the case of several events depositing energy in the same tower of the HF calorimeter. In this case the trigger threshold can eventually be crossed. However, the probability for this is negligible due to the segmentation of the detector combined with the average structure of typical non-selected events.

Multiple simultaneous interactions are counted as one event, leading to the number of detected events being smaller than N_{inel}. The number of pileup events increases with beam intensity, which on the other hand decreases over the time of one fill at the LHC. This happens (mainly) because the lead ions are being used up. According to Eq. (11), P_1 is the probability to detect an event with only one collision. In this convention an event with i collisions should count as $i \times P_1$ but instead is weighted by $1 \times P_i$. Thus, the correction factor of the acceptance for pileup events is

$$f_{\mathrm{PU}} = \frac{\sum\limits_{i=1}^{\infty} i\epsilon_{\mathrm{acc}} \, \mathrm{Pois}(i;\lambda)}{\sum\limits_{i=1}^{\infty} P_i \, \mathrm{Pois}(i;\lambda)} = \frac{\epsilon_{\mathrm{acc}}\lambda}{\sum\limits_{i=1}^{\infty} P_i \, \mathrm{Pois}(i;\lambda)} \; . \qquad (12)$$

The correction factor is calculated as function of the time using time intervals of 23.31 s. The average Poisson probability can be calculated from $\lambda = \mathcal{L}_{\mathrm{inst}}\sigma_{\mathrm{inel}}/(\nu N_{\mathrm{bunches}})$, where $\mathcal{L}_{\mathrm{inst}}$ is the instantaneous luminosity in $\mathrm{Hz}\times\mathrm{b}^{-1}$, $\nu = 11246$ Hz is the orbit frequency and N_{bunches} is the number of colliding bunch pairs (296 for this analysis). The inelastic cross section is the value iteratively determined by the outcome of this analysis: $\sigma_{\mathrm{inel}} = (2.061 \pm 0.029)$ b. The uncertainty from luminosity is not included here since it cancels with the uncertainty of λ. The uncertainty ϵ_{acc}, together with that of the value of the cross section result itself, limits the precision of the pileup correction. The magnitude of the pileup correction is shown in Table 2 for a typical run. While the correction is on the order of 2 %, the induced uncertainty on the cross section is $\approx 0.03\%$.

Table 2: Pileup correction factor f_{PU} for single-arm and double-arm selection efficiencies are listed for instantaneous luminosities (within a time interval of 23.31 s) at the beginning and at the end of a typical run.

	Beginning	End
λ	0.054	0.024
$\mathcal{L}_{\mathrm{inst}}$	$2\ \mu\mathrm{b}^{-1}/23.31\ s$	$0.9\ \mu\mathrm{b}^{-1}/23.31$ s
f_{PU}(single-arm)	1.025	1.011
f_{PU}(double-arm)	1.026	1.011

Electromagnetic Processes

Different types of electromagnetic (EM) inelastic particle production can occur in ultra-peripheral interactions of colliding ions. This effect is modelled with the STARLIGHT event generator, where the electromagnetic fields of the ions are handled by the equivalent-photon (Weizsäcker-Williams) approximation. Photon interactions (Fig. 5, left) can produce low-energy neutral meson states or lepton/antilepton pairs. Such processes are not considered in the analysis since the largest photon-photon inelastic cross section is $\gamma\gamma$ to $\mathrm{e}^+\mathrm{e}^-$ with values, according to the STARLIGHT generator [26], below 1 μb in pPb collisions at 5.5 TeV for final-states where the $\mathrm{e}^\pm$ energies can potentially pass the thresholds on E_{HF}. Furthermore, there are photon-proton interactions (Fig. 5, right), photo-hadronic $\gamma^* + \mathrm{Parton} \to \mathrm{X}$, where the produced particles can deposit significant energy in the HF calorimeter. The exclusive photo-production of vector mesons (without proton breakup) has much smaller cross sections. The STARLIGHT MC was used to generate two samples for the photo-hadronic processes. The first sample uses DPMJET 3 for photodissociative processes, whereas the second one uses PYTHIA.

After applying the HF energy selection in both single-arm and double-arm case, some STARLIGHT events are left (Figs. 1 and 2) with a detection efficiency ϵ_{EM}. The energy deposit in HF is higher on the side where the proton dissociates. The double-arm selection is therefore more suited to discard electromagnetic events. If one assumes that photodissociation processes do not occur in coincidence with other hadronic inelastic (pomeron-pomeron exchange) processes, one can estimate the number of EM events, N_{em}, as

Figure 5: Examples of ultra-peripheral proton-nucleus interactions. Left panel: A quasi-real photon from the field of the lead ion fluctuates into a neutral ρ meson (circle) which interacts with the incoming proton via a colour-singlet state (pomeron exchange) and decays into π^+ and π^- mesons. Right panel: A quasi-real photon γ^* interacts with a parton leading to the break-up of the proton.

$$N_{\mathrm{em}} = N_{\mathrm{inel}} \frac{\sigma_{\mathrm{EM}}}{\sigma_{\mathrm{inel}}} \epsilon_{\mathrm{EM}} = \mathcal{L} \sigma_{\mathrm{EM}} \epsilon_{\mathrm{EM}} \,. \tag{13}$$

Here, the efficiency ϵ_{EM} depends on the requirement on the signal in HF. For the two selection criteria one obtains the visible electromagnetic cross section by averaging the values for STARLIGHT +DPMJET and STARLIGHT +PYTHIA:

$$\frac{N_{\mathrm{em}}}{\mathcal{L}} = \begin{cases} (63 \pm 11)\ \mathrm{mb} & (\text{single-arm } E_{\mathrm{HF}} > 8\ \mathrm{GeV}) \\ (0.33 \pm 0.05)\ \mathrm{mb} & (\text{double-arm } E_{\mathrm{HF}} > 4\ \mathrm{GeV}) \,. \end{cases} \tag{14}$$

The uncertainty on the visible electromagnetic cross section is obtained from the difference $\Delta\,(N_{\mathrm{em}}/\mathcal{L})$ of the two STARLIGHT samples. The uncertainty is taken as the average of $|\Delta\,(N_{\mathrm{em}}/\mathcal{L})|$ obtained by changing the cut on E_{HF} in steps of 0.1 GeV between 2 and 10 GeV. Subtracting the photo-nuclear contribution introduces a correction of about 3.35% and 0.02% for N_{vis} for single-arm and double-arm selection, respectively.

4.4 Cross section corrections

The photo-nuclear correction and the acceptance extrapolation are applied explicitly when the inelastic cross section is derived. The following quantities are defined:

- the *visible* cross section σ_{vis}: the sum of all processes producing events that pass the selection criteria used in this analysis
- the *visible hadronic* cross section $\sigma_{\mathrm{vis,had}}$: *visible* processes that pass the event selection of this analysis without contribution from electromagnetic events.
- the *hadronic inelastic* cross section σ_{inel}: the *visible hadronic* cross section extrapolated to the full phase space.

The amount of noise events that is subtracted from the measurement is $N_{\mathrm{noise}}/\mathcal{L} = 0.10$ b for the single-arm and 0.01 b for the double-arm event selection. Thus, the final correction for noise is about 5.4% and 0.5%. The correction for pileup, averaged over all data, introduces another correction of about 1.8% for both event selections.

The visible cross section is determined by the measurement according to

$$\begin{aligned}\sigma_{\mathrm{vis}} = \frac{N_{\mathrm{vis}}}{\mathcal{L}} &= (N_{\mathrm{cut}} - N_{\mathrm{noise}} + N_{\mathrm{vis}} f_{\mathrm{noise}})\ \frac{f_{\mathrm{PU}}}{\mathcal{L}} \\ &= \frac{1}{\mathcal{L}} \frac{N_{\mathrm{cut}} - N_{\mathrm{noise}}}{1/f_{\mathrm{PU}} - f_{\mathrm{noise}}}\,, \end{aligned} \tag{15}$$

where N_{cut} is the number of recorded events passing the selection on E_{HF}. The term $+N_{\mathrm{vis}} f_{\mathrm{noise}}$ is necessary because events that are selected due to noise but on top have an inelastic collision taking place are removed by N_{noise} even though they contribute to N_{vis}.

Similarly to Eq. (15) the visible hadronic cross section, i.e. without photo-nuclear contribution N_{em}, is obtained from:

$$\sigma_{\mathrm{vis,had}} = \frac{N_{\mathrm{vis,had}}}{\mathcal{L}} = \frac{1}{\mathcal{L}} \frac{N_{\mathrm{cut}} - N_{\mathrm{noise}} - N_{\mathrm{em}}}{1/f_{\mathrm{PU}} - f_{\mathrm{noise}}}\,. \tag{16}$$

Finally the inelastic cross section is corrected for the limited acceptance, by dividing by the efficiency ϵ_{acc}:

$$\sigma_{\mathrm{inel}} = \frac{\sigma_{\mathrm{vis,had}}}{\epsilon_{\mathrm{acc}}}\,. \tag{17}$$

5 Systematic Uncertainties

There are a number of sources for systematic uncertainty that need to be considered. Table 3 lists the value of each source of systematic uncertainty:

- The uncertainty of the integrated luminosity has been analysed with van-der-Meer scans in a dedicated analysis (Section 3). The uncertainty was determined to be 3.5%. This is the largest source of uncertainty on the cross section.
- The uncertainty on the extrapolation to the full phase space, Eq. (7), gives 0.5% and 1.6% for single-arm and double-arm selection, respectively. Since diffraction in proton-lead collisions is not well studied the extrapolation was also tested against an increased diffractive cross section in EPOS-LHC and QGSJETII-04 (see Section 4.3). Reevaluation of the full analysis with the modified generators results in an increase of 1.5% and 2.0% of σ_{inel} for the single-arm and double-arm event selection, respectively.
- The effect of the uncertainty of the photo-nuclear contribution for the single-arm event selection is 0.2% while for the double-arm event selection it is $< 0.05\%$.
- Taking the modelling uncertainty of the HF simulation into account results in an additional 1.7% and 0.8% uncertainty on the final cross section, for single-arm and double-arm selection respectively. The central values for the corrections were obtained from the rescaled simulation results and the difference to the non-rescaled simulations serves as uncertainty in both directions.
- The event selection was modified to $E_{\mathrm{HF}} > 10$ GeV (single-arm selection) and 5 GeV (double-arm selection) to achieve a smaller noise contribution. The influence on the measured cross section was checked and the full difference is added as systematic

uncertainty. This amounts to 0.6% and 0.2% for single-arm and double-arm selection, respectively.

- The run-by-run variations of f_{noise} are taken into account as a systematic uncertainty. This results in 1.2% uncertainty for the single-arm selection and 0.2% for the double-arm selection.

All systematic uncertainties are added in quadrature.

The non-luminosity related uncertainties are small. It is interesting that, despite the differences in the individual contributions to the uncertainties for the double-arm and single-arm analyses, the uncertainties for both selections, without considering the luminosity contribution, add up to roughly 2.7%.

Table 3: Systematic uncertainties on σ_{inel} for two event selection methods.

Source of uncertainty		Single-arm	Double-arm
Luminosity measurement		3.5%	3.5%
Pileup uncertainty		<0.1%	<0.1%
Extrapolation $\sigma_{\text{vis,had}} \rightarrow \sigma_{\text{inel}}$	Model difference	0.5%	1.6%
	optimised σ_{diff}	1.5%	2.0%
Photo-nuclear correction		0.2%	<0.1%
Modelling uncertainty		1.7%	0.8%
Event selection		0.6%	0.2%
Noise subtraction		1.2%	0.2%
Total without $\sigma_{\mathcal{L}}$		2.7%	2.7%
Total with $\sigma_{\mathcal{L}}$		4.4%	4.4%
Both selections combined		4.0%	

6 Results

The cross section is computed, using Eq. (17), as the weighted average over all 23.31 s periods of each run (cf. Fig. 6, left) and subsequently calculating the weighted average over all runs (see Fig. 6, right). The standard deviation of the weighted mean, which is derived from the Poisson distributed number of events in each 23.31 s data taking period and each run, only introduces a small statistical uncertainty of 0.003 b. The difference of the beam direction (pPb or Pbp) does not indicate any visible difference and confirms the robustness of the measurement with respect to any possible detector differences in the direction of the two beams. The obtained values for the visible, visible hadronic, and hadronic inelastic cross sections defined respectively in Equations (15), (16), and (17) are listed in Table 4.

Table 4: The visible cross section (noise and pileup corrected), visible hadronic cross section (as visible but without photon-proton contribution) and hadronic inelastic cross section (as hadronic but extrapolated to ideal acceptance) obtained by the two different event selections.

Selection	σ_{vis} (b)	$\sigma_{\text{vis,had}}$ (b)	σ_{inel} (b)
$E_{\text{HF}} > 8$ GeV (single-arm)	2.003	1.938	2.063
$E_{\text{HF}} > 4$ GeV (double-arm)	1.873	1.873	2.059

The value of the visible cross section is 130 mb larger for the single-arm selection than for the double-arm selection. After the photo-nuclear correction to the visible hadronic cross section there is a difference of 65 mb. When also the extrapolation to the full phase space is applied, a

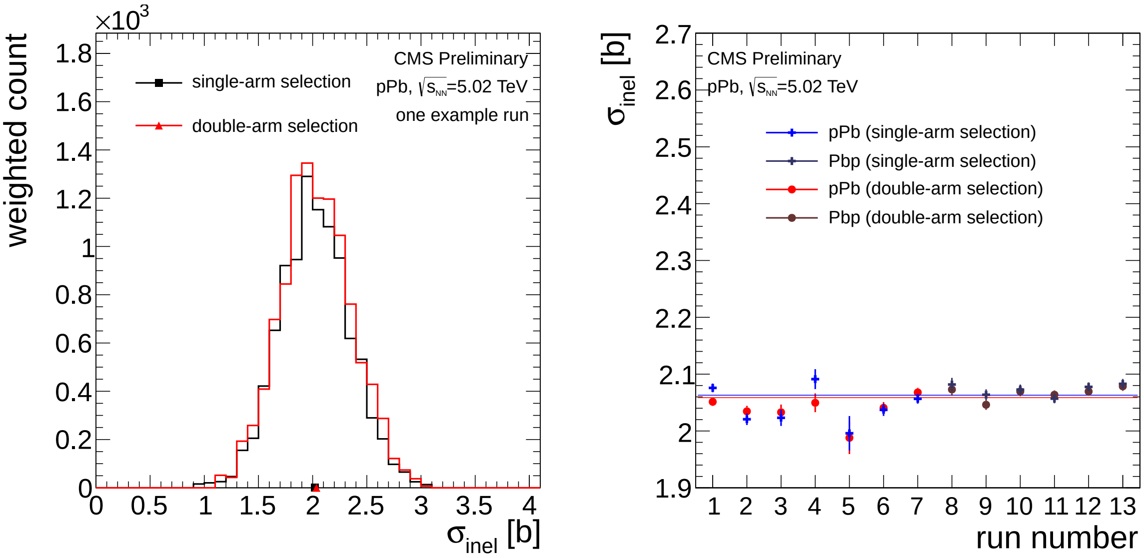

Figure 6: Left panel: Inelastic cross section values derived from Eq. (17) for one example run. One value for each 23.31 s period is added with weight 1/variance determined by the Poisson distribution. The averages of the two event selections are indicated by markers on the x-axis. Right panel: Measured inelastic cross sections for the two selection criteria as a function of analysed runs (the horizontal lines show the weighted mean of the values for each event selection criterion).

difference of only 4 mb remains (cf. Fig. 7). The good agreement shows that the corrections are well understood. The result of the measurements is:

$$\sigma_{\text{inel,single}} = (2.063 \pm 0.003(\text{stat.}) \pm 0.056(\text{syst.}) \pm 0.072(\text{lumi.}))\ \text{b} \quad \text{(single-arm selection)} \tag{18}$$

$$\sigma_{\text{inel,double}} = (2.059 \pm 0.003(\text{stat.}) \pm 0.056(\text{syst.}) \pm 0.072(\text{lumi.}))\ \text{b} \quad \text{(double-arm selection).} \tag{19}$$

The two selections are combined by taking the average $\sigma_{\text{inel}} = (\sigma_{\text{inel,single}} + \sigma_{\text{inel,double}})/2$.

The statistical uncertainties and the uncertainty on the luminosity are correlated. For the remaining systematic uncertainties the correlation is less direct and they are taken to be uncorrelated. Hence, the combined uncertainties are obtained by averaging the statistical and the luminosity uncertainties, and by adding the remaining systematic uncertainties in quadrature (see last row of Table 3).

This yields a final result for the hadronic inelastic cross section of

$$\sigma_{\text{inel}} = (2.061 \pm 0.003(\text{stat.}) \pm 0.039(\text{syst.}) \pm 0.072(\text{lumi.}))\ \text{b}\ . \tag{20}$$

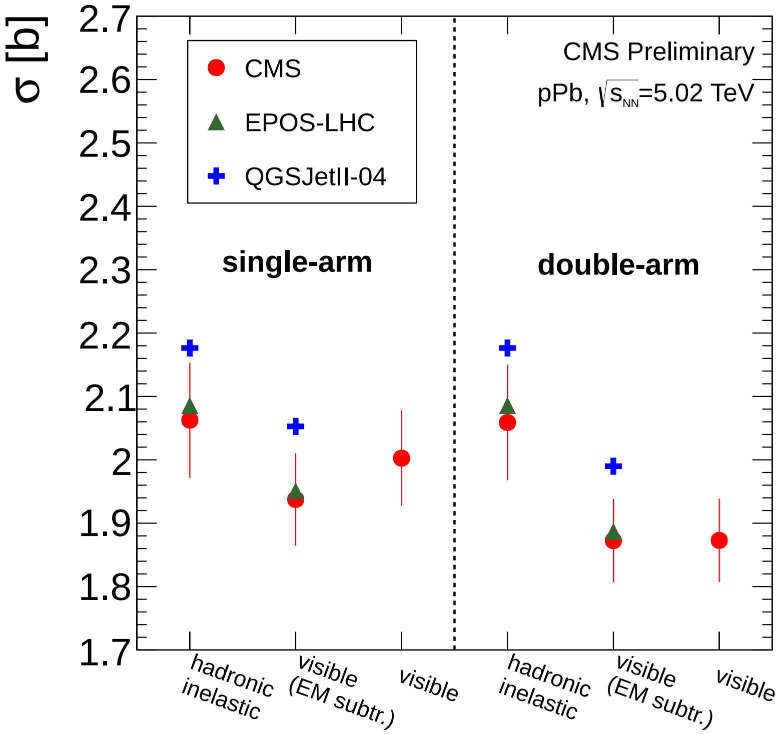

Figure 7: The measured proton-lead cross section for visible, visible hadronic, and hadronic inelastic contribution. The systematic uncertainty on σ_{inel} is shown as defined in Table 3. For $\sigma_{\text{vis,had}}$ the extrapolation and modelling uncertainties do not enter. In addition, the uncertainty on electromagnetic events does not enter for σ_{vis}. Model predictions from the hadronic interaction models EPOS-LHC and QGSJETII-04 are given for the visible hadronic and hadronic inelastic cross section.

7 Conclusion

The hadronic inelastic proton-lead cross section has been measured for pPb collisions at $\sqrt{s_{\mathrm{NN}}} = 5.02$ TeV. The final result of the measurement is shown in Fig. 8 compared to various theoretical predictions. Foremost, the measured hadronic inelastic cross section is compared to the standard Glauber calculation with 70 mb as input for the proton-proton cross section. The proton-proton cross section was derived by the COMPETE parametrisation [27] including the TOTEM measurement at 7 TeV. With this as input, it follows a prediction of the Glauber theory of $\sigma_{\mathrm{inel}} = (2.13 \pm 0.04)$ b which is compatible with the result of this analysis. This points to the fact that screening corrections and anti-screening effects are similar in magnitude (but opposite in sign) for pPb collisions at 5.02 TeV. Thus, the Glauber calculation gives a reasonable result within the precision of the measurement. Furthermore, the other model predictions are also compatible with the measurements given the experimental uncertainties. Only QGSJETII-04 predicts a value slightly above the upper uncertainty bound of this measurement.

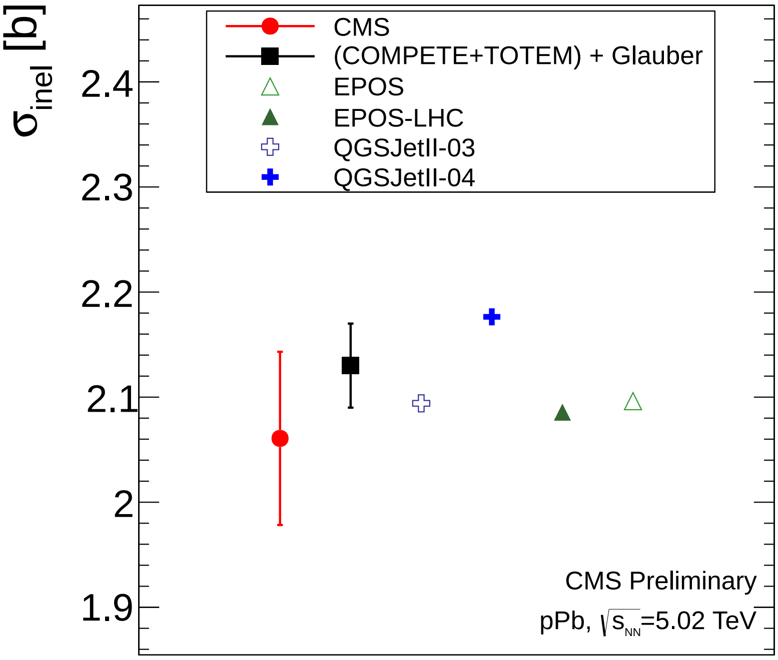

Figure 8: Measured proton-lead hadronic inelastic cross section compared to model predictions.

The values of the pPb hadronic inelastic cross section measured as a function of the nucleon-nucleon centre-of-mass energy are shown in Fig. 9. The lowest energy data correspond to the absorption cross section measured at IHEP [28] and FNAL [29]. The intermediate-energy values up to 3.5 TeV correspond to cosmic ray data on a fixed lead target [30]. The model predictions reproduce the experimental data with good accuracy.

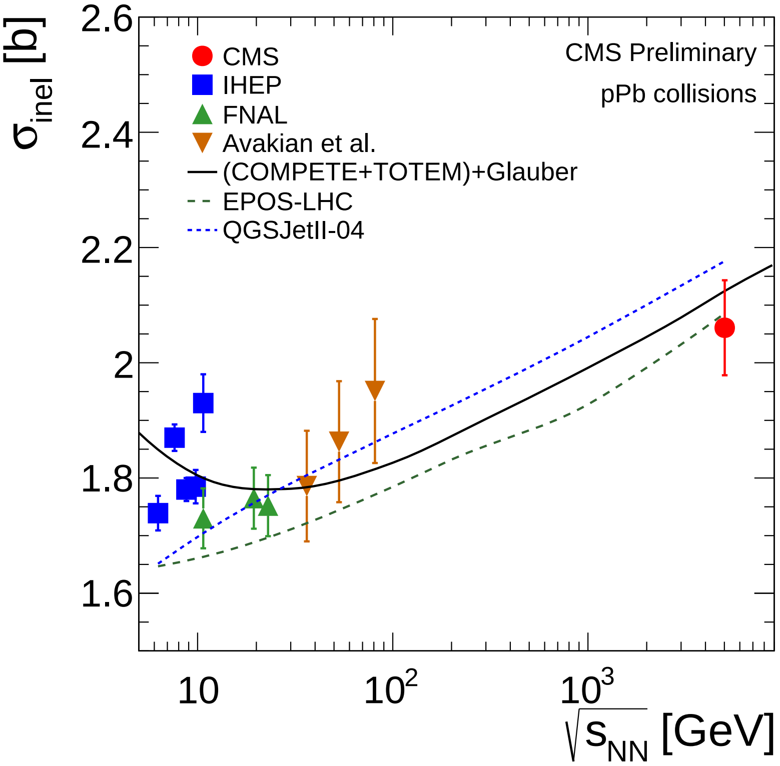

Figure 9: Hadronic inelastic proton-lead cross section as a function of centre-of-mass energy. The data are from this work (CMS) and [28–30]. The lines show predictions by the hadronic interaction models EPOS-LHC, QGSJETII-04 and a Glauber calculation based on the pp cross section from the COMPETE fit that has been extended by the TOTEM measurement at a centre-of-mass energy of 7 TeV.

References

[1] I. Sarcevic, S. D. Ellis, and P. Carruthers, "QCD minijet cross-sections", *Phys. Rev. D* **40** (1989) 1446, `doi:10.1103/PhysRevD.40.1446`.

[2] R. J. Glauber, "Cross-sections in deuterium at high-energies", *Phys. Rev.* **100** (1955) 242, `doi:10.1103/PhysRev.100.242`.

[3] R. J. Glauber and G. Matthiae, "High-energy scattering of protons by nuclei", *Nucl. Phys. B* **21** (1970) 135, `doi:10.1016/0550-3213(70)90511-0`.

[4] V. N. Gribov, "A reggeon diagram technique", *Sov. Phys. JETP* **26** (1968) 414.

[5] T. Sjostrand, S. Mrenna, and P. Z. Skands, "A Brief Introduction to PYTHIA 8.1", *Comput. Phys. Commun.* **178** (2008) 852, `doi:10.1016/j.cpc.2008.01.036`, `arXiv:0710.3820`.

[6] X.-N. Wang and M. Gyulassy, "HIJING: A Monte Carlo model for multiple jet production in p p, p A and A A collisions", *Phys. Rev. D* **44** (1991) 3501, `doi:10.1103/PhysRevD.44.3501`.

[7] K. Werner, F.-M. Liu, and T. Pierog, "Parton ladder splitting and the rapidity dependence of transverse momentum spectra in deuteron-gold collisions at RHIC", *Phys. Rev. C* **74** (2006) 044902, `doi:10.1103/PhysRevC.74.044902`, `arXiv:hep-ph/0506232`.

[8] S. Ostapchenko, "Air shower calculations with QGSJET-II: Effects of Pomeron loops", *Nucl. Phys. Proc. Suppl.* **196** (2009) 90, `doi:10.1016/j.nuclphysbps.2009.09.014`.

[9] T. K. Gaisser and F. Halzen, "Soft Hard Scattering in the TeV Range", *Phys. Rev. Lett.* **54** (1985) 1754, `doi:10.1103/PhysRevLett.54.1754`.

[10] L. Durand and P. Hong, "QCD and Rising Total Cross-Sections", *Phys. Rev. Lett.* **58** (1987) 303, `doi:10.1103/PhysRevLett.58.303`.

[11] D. G. d'Enterria, "Hard scattering cross-sections at LHC in the Glauber approach: From pp to pA and AA collisions", `arXiv:nucl-ex/0302016`.

[12] M. L. Miller, K. Reygers, S. J. Sanders, and P. Steinberg, "Glauber modeling in high energy nuclear collisions", *Ann. Rev. Nucl. Part. Sci.* **57** (2007) 205, `doi:10.1146/annurev.nucl.57.090506.123020`, `arXiv:nucl-ex/0701025`.

[13] M. L. Good and W. D. Walker, "Diffraction disssociation of beam particles", *Phys. Rev.* **120** (1960) 1857, `doi:10.1103/PhysRev.120.1857`.

[14] C. Ciofi degli Atti et al., "Number of Collisions in the Glauber Model and Beyond", *Phys. Rev. C* **84** (2011) 025205, `doi:10.1103/PhysRevC.84.025205`, `arXiv:1105.1080`.

[15] M. Alvioli et al., "Nucleon momentum distributions, their spin-isospin dependence and short-range correlations", *Phys. Rev. C* **87** (2013) 034603, `doi:10.1103/PhysRevC.87.034603`, `arXiv:1211.0134`.

[16] CMS Collaboration, "Study of W boson production in PbPb and pp collisions at $\sqrt{s_{NN}} = 2.76$ TeV", *Phys. Lett. B* **715** (2012) 66, `doi:10.1016/j.physletb.2012.07.025`, `arXiv:1205.6334`.

[17] Pierre Auger Collaboration, “Measurement of the proton-air cross-section at $\sqrt{s} = 57$ TeV with the Pierre Auger Observatory”, *Phys. Rev. Lett.* **109** (2012) 062002, `doi:10.1103/PhysRevLett.109.062002`, `arXiv:1208.1520`.

[18] N. N. Kalmykov and S. S. Ostapchenko, “The Nucleus-nucleus interaction, nuclear fragmentation, and fluctuations of extensive air showers”, *Phys. Atom. Nucl.* **56** (1993) 346.

[19] CMS Collaboration, “The CMS experiment at the CERN LHC”, *JINST* **3** (2008) S08004, `doi:10.1088/1748-0221/3/08/S08004`.

[20] CMS HF Calorimeters Collaboration, “CMS hadronic forward calorimeter”, *Nucl. Phys. Proc. Suppl.* **61B** (1998) 41.

[21] S. van der Meer, “Calibration of the effective beam height in the ISR”, Technical Report CERN-ISR-PO-68-31. ISR-PO-68-31, CERN, Geneva, (1968).

[22] F. J. Decker, “Beam distributions beyond RMS”, *SLAC-PUB-6684, C94-10-02.1* (1994).

[23] CMS Collaboration, “CMS Luminosity Based on Pixel Cluster Counting - Summer 2013 Update”, Technical Report CMS-PAS-LUM-13-001, CERN, Geneva, (2013).

[24] S. Klein and J. Nystrand, “Exclusive vector meson production in relativistic heavy ion collisions”, *Phys. Rev. C* **60** (1999) 014903, `doi:10.1103/PhysRevC.60.014903`, `arXiv:hep-ph/9902259`.

[25] S. Roesler, R. Engel, and J. Ranft, “The Monte Carlo event generator DPMJET-III”, `arXiv:hep-ph/0012252` (2000).

[26] A. J. Baltz, Y. Gorbunov, S. R. Klein, and J. Nystrand, “Two-Photon Interactions with Nuclear Breakup in Relativistic Heavy Ion Collisions”, *Phys. Rev. C* **80** (2009) 044902, `doi:10.1103/PhysRevC.80.044902`, `arXiv:0907.1214`.

[27] COMPETE Collaboration, “Analytic parametrizations of the nonperturbative pomeron and QCD inspired models”, `arXiv:hep-ph/0110170`.

[28] S. P. Denisov et al., “Absorption cross-sections for pions, kaons, protons and anti-protons on complex nuclei in the 6-GeV/c to 60-GeV/c momentum range”, *Nucl. Phys. B* **61** (1973) 62, `doi:10.1016/0550-3213(73)90351-9`.

[29] A. S. Carroll et al., “Absorption Cross-Sections of $\pi^{\pm}$, $\mathrm{K}^{\pm}$, p and anti-p on Nuclei Between 60 GeV/c and 280 GeV/c”, *Phys. Lett. B* **80** (1979) 319, `doi:10.1016/0370-2693(79)90226-0`.

[30] V. V. Avakian et al., “Determining inelastic interaction cross-sections for nucleons and pions incident on carbon and lead nuclei at 0.5 TeV - 5 TeV”, *Bull. Russ. Acad. Sci. Phys.* **50N11** (1986) 4.